

1 The Silicon Vertex Detector of the Belle II Experiment

2 Y. Uematsu^a, K. Adamczyk^t, L. Aggarwal^l, H. Aihara^q, T. Aziz^j, S. Bacher^t,
3 S. Bahinipati^f, G. Batignani^{k,l}, J. Baudot^e, P. K. Behera^g, S. Bettarini^{k,l},
4 T. Bilka^c, A. Bozek^t, F. Buchsteiner^b, G. Casarosa^{k,l}, L. Corona^{k,l}, T. Czank^p,
5 S. B. Das^h, G. Dujany^e, C. Finck^e, F. Forti^{k,l}, M. Friedl^b, A. Gabrielli^{m,n},
6 E. Ganiev^{m,n}, B. Gobboⁿ, S. Halder^j, K. Hara^{r,o}, S. Hazra^j, T. Higuchi^p,
7 C. Irmeler^b, A. Ishikawa^{r,o}, H. B. Jeon^s, Y. Jin^{m,n}, C. Joo^p, M. Kaleta^t,
8 A. B. Kaliyar^j, J. Kandra^c, K. H. Kang^s, P. Kapusta^t, P. Kodyš^c, T. Kohriki^r,
9 M. Kumar^h, R. Kumarⁱ, C. La Licata^p, K. Lalwani^h, R. Le Boucher^d,
10 S. C. Lee^s, J. Libby^g, L. Martel^e, L. Massacesi^{k,l}, S. N. Mayekar^j,
11 G. B. Mohanty^j, T. Morii^p, K. R. Nakamura^{r,o}, Z. Natkaniec^t, Y. Onuki^q,
12 W. Ostrowicz^t, A. Paladino^{k,l}, E. Paoloni^{k,l}, H. Park^s, G. Polat^d, K. K. Rao^j,
13 I. Ripp-Baudot^e, G. Rizzo^{k,l}, D. Sahoo^j, C. Schwanda^b, J. Serrano^d,
14 J. Suzuki^r, S. Tanaka^{r,o}, H. Tanigawa^q, R. Thalmeier^b, R. Tiwari^j,
15 T. Tsuboyama^{r,o}, O. Verbycka^t, L. Vitale^{m,n}, K. Wan^q, Z. Wang^q, J. Webb^a,
16 J. Wiechczynski^l, H. Yin^b, L. Zani^d,

17 (Belle-II SVD Collaboration)

18 ^a*School of Physics, University of Melbourne, Melbourne, Victoria 3010, Australia*

19 ^b*Institute of High Energy Physics, Austrian Academy of Sciences, 1050 Vienna, Austria*

20 ^c*Faculty of Mathematics and Physics, Charles University, 121 16 Prague, Czech Republic*

21 ^d*Aix Marseille Université, CNRS/IN2P3, CPPM, 13288 Marseille, France*

22 ^e*IPHC, UMR 7178, Université de Strasbourg, CNRS, 67037 Strasbourg, France*

23 ^f*Indian Institute of Technology Bhubaneswar, Satya Nagar, India*

24 ^g*Indian Institute of Technology Madras, Chennai 600036, India*

25 ^h*Malaviya National Institute of Technology Jaipur, Jaipur 302017, India*

26 ⁱ*Punjab Agricultural University, Ludhiana 141004, India*

27 ^j*Tata Institute of Fundamental Research, Mumbai 400005, India*

28 ^k*Dipartimento di Fisica, Università di Pisa, I-56127 Pisa, Italy*

29 ^l*INFN Sezione di Pisa, I-56127 Pisa, Italy*

30 ^m*Dipartimento di Fisica, Università di Trieste, I-34127 Trieste, Italy*

31 ⁿ*INFN Sezione di Trieste, I-34127 Trieste, Italy*

32 ^o*The Graduate University for Advanced Studies (SOKENDAI), Hayama 240-0193, Japan*

33 ^p*Kavli Institute for the Physics and Mathematics of the Universe (WPI), University of*

34 *Tokyo, Kashiwa 277-8583, Japan*

35 ^q*Department of Physics, University of Tokyo, Tokyo 113-0033, Japan*

36 ^r*High Energy Accelerator Research Organization (KEK), Tsukuba 305-0801, Japan*

37 ^s*Department of Physics, Kyungpook National University, Daegu 41566, Korea*

38 ^t*H. Niewodniczanski Institute of Nuclear Physics, Krakow 31-342, Poland*

39 Abstract

40 The Silicon Vertex Detector (SVD) is a part of the vertex detector in the
41 Belle II experiment at the SuperKEKB collider (KEK, Japan). Since the start
42 of data taking in spring 2019, the SVD has been operating stably and reliably

43 with a high signal-to-noise ratio and hit efficiency, achieving good spatial resolu-
44 tion and high track reconstruction efficiency. The hit occupancy, which mostly
45 comes from the beam-related background, is currently about 0.5% in the in-
46 nermost layer, causing no impact on the SVD performance. In anticipation of
47 the operation at higher luminosity in the next years, two strategies to sustain
48 the tracking performance in future high beam background conditions have been
49 developed and tested on data. One is to reduce the number of signal waveform
50 samples to decrease dead time, data size, and occupancy. The other is to utilize
51 the good hit-time resolution to reject the beam background hits. We also mea-
52 sured the radiation effects on the sensor current, strip noise, and full depletion
53 voltage caused during the first two and a half years of operation. The results
54 show no detrimental effect on the SVD performance.

55 *Keywords:* Silicon strip detector, Vertex detector, Tracking detector, Belle II

56 1. Introduction

57 The Belle II experiment [1] aims to probe new physics beyond the Standard
58 Model in high-luminosity e^+e^- collisions at the SuperKEKB collider (KEK,
59 Japan) [2]. SuperKEKB consists of the following components: injector LINAC,
60 positron damping ring, and main storage ring with the electron and positron
61 beamlines. The Belle II detector is located at the interaction point (IP) of
62 the two beamlines. The main collision energy in the center-of-mass system is
63 10.58 GeV on the $\Upsilon(4S)$ resonance, which enables various physics programs
64 based on the large samples of B mesons, τ leptons, and D mesons. Also, the
65 asymmetric energy of the 7 GeV electron beam and 4 GeV positron beam is
66 adopted for time-dependent CP violation measurements. The target of Su-
67 perKEKB is to accumulate an integrated luminosity of 50 ab^{-1} with peak lu-
68 minosity of about $6 \times 10^{35} \text{ cm}^{-2}\text{s}^{-1}$. In June 2021, SuperKEKB recorded the
69 world's highest instantaneous luminosity of $3.1 \times 10^{34} \text{ cm}^{-2}\text{s}^{-1}$. The data accu-
70 mulated before July 2021 corresponds to an integrated luminosity of 213 fb^{-1} .

71 The Vertex Detector (VXD) is the innermost detector in the Belle II detector

72 system. The VXD has six layers: the inner two layers (layers 1 and 2) are the
 73 Pixel Detector (PXD), and the outer four layers (layers 3 to 6) are the Silicon
 74 Vertex Detector (SVD). The schematic cross-sectional view of the VXD is shown
 75 in Fig. 1. The PXD consists of DEPFET pixel sensors, and its innermost radius
 76 is 1.4 cm from the IP. A detailed description of the SVD appears in Sec. 2.

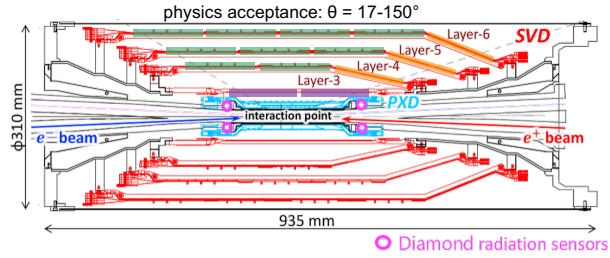


Figure 1: Schematic cross-sectional view of the VXD. The SVD is in red, the PXD in light-blue, and the IP beam pipe diamonds in pink circles. The locations of the three types of DSSDs are indicated by boxes in three colors: purple for small sensors, green for large sensors, and orange for trapezoidal sensors as described in Tab. 1.

77 Besides the VXD, diamond sensors [3] are mounted on the IP beam pipe and
 78 the bellows pipes outside of the VXD. The pink circles in Fig. 1 indicate the
 79 locations of the diamond sensors on the IP beam pipe. They measure the dose
 80 rates in these locations. The measured doses are used to estimate the dose in
 81 the SVD. They also send beam abort requests to SuperKEKB if the radiation
 82 level gets too high to avoid severe damage to the detector.

83 2. Belle II Silicon Vertex Detector

84 The SVD is crucial for extrapolating the tracks to the PXD. This task is
 85 essential for measuring the decay vertices with the PXD and pointing at a region-
 86 of-interest limiting the PXD readout volume. Other roles of the SVD are the
 87 standalone track reconstruction of low-momentum charged particles and their
 88 particle identification using ionization energy deposits. The SVD also plays a
 89 critical role in the decay vertex measurement in the case of long-lived particles
 90 like K_S mesons, which decay inside the SVD volume.

91 The SVD [4] consists of four layers of double-sided silicon strip detectors
 92 (DSSDs). The material budget of the SVD is about 0.7% of a radiation length
 93 per layer. The aluminum readout strips are AC-coupled to every other n/p-
 94 side strips (electrodes) on the n-type substrate over the silicon oxide layer. On
 95 each DSSD plane, a local coordinate is defined with u and v : u -axis along n-side
 96 strips and v -axis perpendicular to u -axis. In other words, p-side strips and n-side
 97 strips provide u and v information, respectively. In the cylindrical coordinate, u
 98 corresponds to $r-\varphi$ information and v corresponds to z information. The SVD
 99 consists of three types of sensors: “small” sensors in layer 3, “large” sensors in
 100 the barrel region of layers 4, 5, and 6, and “trapezoidal” sensors in the forward
 101 region of layers 4, 5, and 6, which is slanted. They are indicated in blue, green,
 102 and orange boxes in Fig. 1. The dimensions for these three types of sensors
 103 are summarized in Tab. 1. The sensors are manufactured by two companies:
 104 the small and large sensors by Hamamatsu and trapezoidal sensors by Micron.
 105 The full depletion voltage is 60 V for Hamamatsu sensors and 20 V for Micron
 106 sensors; both types of sensors are operated at 100 V. In total, 172 sensors are
 107 assembled, corresponding to a total sensor area of 1.2 m² and approximately
 108 224,000 readout strips.

	Small	Large	Trapezoidal
No. of u/p-strips	768	768	768
u/p-strip pitch	50 μm	75 μm	50–75 μm
No. of v/n-strips	768	512	512
v/n-strip pitch	160 μm	240 μm	240 μm
Thickness	320 μm	300 μm	300 μm
Manufacturer	Hamamatsu		Micron

Table 1: Table of the dimensions for the three types of sensors. Only readout strips are taken into account for number of strips and strip pitch.

109 The front-end ASIC used in the SVD is APV25 [5], which was originally
 110 developed for the CMS silicon tracker. The APV25 is radiation hard for a dose

111 up to 100 Mrad radiation. It has 128 channel inputs and shapers for each channel
112 with a shaping time of about 50 ns. For the SVD, the APV25 is operated in
113 “multi-peak” mode. The mechanism of the data sampling in the multi-peak
114 mode is explained in Fig. 2. The chip samples the height of the signal waveform
115 with the 32 MHz clock (31 ns period) and stores each sample’s information in an
116 analog ring buffer. Since the bunch-crossing frequency is eight times faster than
117 the sampling clock, the stored samples are not synchronous to the beam collision,
118 in contrast to CMS, which motivates operation in the multi-peak mode. In the
119 present readout configuration (the six-samples mode), at every reception of the
120 Belle II global Level-1 trigger, the chip reads out six successive samples of the
121 signal waveform stored in the buffers. The six-samples mode offers enough time
122 window ($6 \times 31 \text{ ns} = 187 \text{ ns}$) to accommodate large timing shifts of the trigger. In
123 preparation for operation with higher luminosity, where background occupancy,
124 trigger dead-time, and the data size increase, we developed the three/six-mixed
125 acquisition mode (mixed-mode). The mixed-mode is a new method to read out
126 the signal samples from the APV25, in which the number of the samples changes
127 between three and six in each event, depending on the timing precision of each
128 Level-1 trigger signal in that event. For triggers with good timing precision,
129 three-samples data are read out and the data have half time window and half
130 data size compared to ones of six-samples data, resulting in the reduction of the
131 effect due to higher luminosity. This functionality was already implemented in
132 the running system and confirmed by a few hours of smooth physics data-taking.
133 Before we start to use the mixed-mode, the effect on the performance due to
134 the change of the acquisition mode is to be assessed. As the first step, the effect
135 in the hit efficiency was evaluated as described in Sec. 3.

136 The APV25 chips are mounted on each middle sensor (chip-on-sensor con-
137 cept) with thermal isolation foam in between. The merit of this concept is
138 shorter signal propagation length, leading to smaller capacitance of the signal
139 line and hence reduced noise level. To minimize the material budget the APV25
140 chips on the sensor are thinned down to 100 μm . APV25s are mounted on a
141 single side of the sensor and readout of the signals is from the other side via

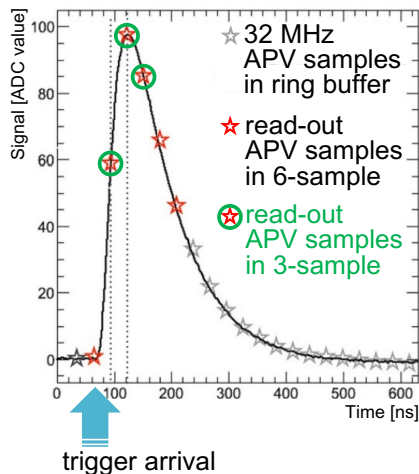


Figure 2: Example of sampling in the “multi-peak” mode of APV25. The black line shows the signal waveform after the CR-RC shaper circuit. The stars show the sampled signal height recorded in the analog ring buffer according to the 32 MHz sampling clock. The red stars indicate the six successive samples read out at the trigger reception in the six-samples mode. The red stars with a green circle indicate the samples read out in the three-samples acquisition.

142 wrapped flexible printed circuits. The power consumption of the APV25 chip
 143 is 0.4 W/chip and in total 700 W in the entire SVD. The chips are chilled by
 144 bi-phase -20°C CO_2 .

145 3. Performance

146 The SVD was combined with the PXD to complete the VXD assembly in
 147 October 2018, and the VXD was installed to the Belle II detector system in
 148 November 2018. Since March 2019, the SVD has been operating reliably and
 149 smoothly for two and a half years. The total fraction of masked strips is about
 150 1%. There was only one issue where one APV25 chip (out of 1,748 chips) was
 151 disabled during the spring of 2019, which was remediated by reconnecting a
 152 cable in the summer of 2019.

153 The SVD has also demonstrated stable and excellent performance [6]. The
 154 hit efficiency is continuously over 99% in most of the sensors. The cluster

155 charge distributions are also reasonable. On the u/p-side, the most probable
 156 values agree with the calculated charge amount induced by MIPs within the
 157 uncertainty in calibration. On the v/n-side, 10–30% of the collected charge is
 158 lost compared to MIP due to the smaller inter-strip capacitance of the floating
 159 strips with larger strip pitches than the u/p-side. The most probable values of
 160 the cluster signal-to-noise ratio distributions range from 13 to 30.

161 We measured the cluster position resolution by analyzing the $e^+e^- \rightarrow \mu^+\mu^-$
 162 data [7]. The cluster position resolution is estimated from the residual between
 163 the cluster position and the track position not biased by the target cluster after
 164 subtracting the effect of the track extrapolation error. The cluster position
 165 resolutions for different incident angles are shown in Fig. 3. For normal incident
 166 tracks, it agrees with the expectations from the strip pitch including floating
 167 strips. For tracks with an incident angle, it is expected to get a better resolution,
 168 which is indeed the case in the v/n-side results. However, this effect is not
 169 observed on the u/p-side, and the study is still ongoing to improve the cluster
 170 position estimation.

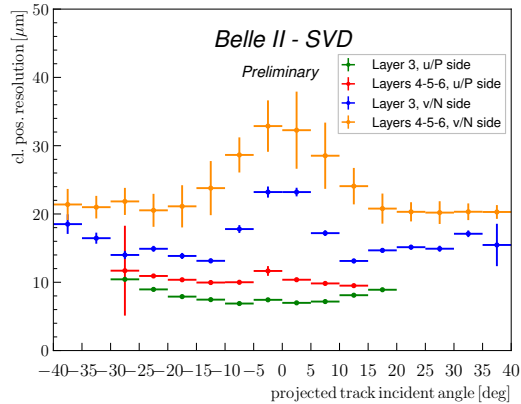


Figure 3: The SVD cluster position resolution depending on the projected track incident angle. The green (blue) plot shows the resolution in the u/p-side (n/v-side) of layer-3 sensors, and the red (yellow) one shows the u/p-side (n/v-side) of layers-4, 5, and 6 sensors.

171 The cluster hit-time resolution was also evaluated in candidate hadronic

172 events¹ using the reference event time estimated by the Central Drift Chamber
 173 (CDC) outside of the SVD. The error on the event time, about 0.7 ns, was
 174 subtracted to evaluate the intrinsic SVD hit-time resolution. The resulting
 175 resolution is 2.9 ns on the u/p-side and 2.4 ns on the v/n-side. With such
 176 precise hit-time information, it is possible to reject off-time background hits
 177 efficiently. The hit-time distributions for signal² and background³ are shown
 178 in Fig. 4. The signal distribution has a narrow peak, while the background
 179 hit-time distribution is broad and almost flat in the signal peak region. The
 180 separation power of the hit-time is high, as expected. For example, if we reject
 181 hits with the hit-time less than -38 ns in this plot, we can reject 45% of the
 182 background hits while keeping 99% of the signal hits. The background rejection
 183 based on the hit-time is essential to sustain the good tracking performance in
 184 the future high beam background condition.

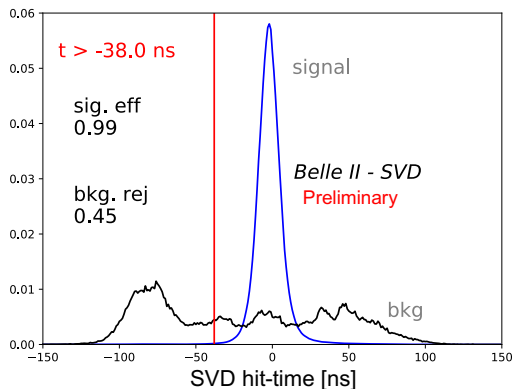


Figure 4: Example of the background hit rejection using hit-time. The blue distribution shows the signal, and the black distribution shows the background. Assuming the hit-time cut at -38 ns, the signal hit efficiency of 99% and the background hit rejection of 45% are achieved.

185 The performance in three-samples data was compared with that in six-
 186 samples data to evaluate the performance in the mixed-mode. If the trigger

¹The events with more than three good tracks and not like Bhabha scattering.

²The clusters found to be used in the tracks in the hadronic events.

³The clusters in events triggered by delayed-Bhabha pseudo-random trigger.

187 timing has no deviation, the three-samples data will show comparable perfor-
 188 mance to the six-samples data because the relevant part of the signal waveform
 189 to evaluate the necessary signal properties, which are the signal height and the
 190 signal timing, can be accommodated in the three-sample's time window. How-
 191 ever, when the trigger has a jitter and the timing shift happens, some part of
 192 the signal waveform can be out of the three-sample's time window, and the
 193 reconstruction performance deteriorates. We examined the effect on the hit ef-
 194 ficiency as a function of the trigger timing shift. The effect is evaluated by the
 195 relative hit efficiency, which is defined as the ratio of the hit efficiency in the
 196 three-samples data to the one in the six-samples data. For this study, the three-
 197 samples data are emulated in the offline analysis from the six-samples data by
 198 selecting consecutive three samples at a fixed latency with respect to the L1
 199 trigger signal. The trigger timing shift is evaluated by the CDC event time.
 200 The resulting relative efficiencies as a function of the trigger timing shift in the
 201 hadronic events are shown in Fig. 5. The decreasing trend is observed for the
 202 shift of the trigger timing, as expected. As a result, the relative efficiency is
 203 over 99.9% for the trigger timing shift within ± 30 ns, which is almost all the
 204 events.

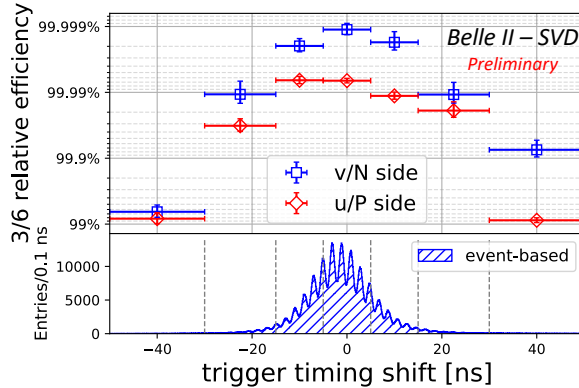


Figure 5: The relative hit efficiencies (the ratios of the hit efficiency in the three-samples data to the one in the six-samples data) as a function of the trigger timing shift for v/n-side (blue square) and u/p-side (red diamond). The positive (negative) trigger timing shift corresponds to early (late) trigger timing.

205 4. Beam-related background effects on SVD

206 The beam-related background increases the hit occupancy of the SVD, which
207 in turn degrades the tracking performance. Considering this performance degra-
208 dation, we set the occupancy limit in layer-3 sensors to be about 3%, which will
209 be loosened roughly by a factor of two after we apply the hit-time rejection
210 described in Sec. 3. With the current luminosity, the average hit occupancy in
211 layer-3 sensors is less than 0.5%. However, the projection of the hit occupancy
212 at the luminosity of $8 \times 10^{35} \text{ cm}^{-2}\text{s}^{-1}$ is about 3% in layer-3 sensors. The pro-
213 jected occupancy comes from the Monte Carlo (MC) simulation scaled by the
214 data/MC ratio determined from the beam background data of the current beam
215 optics. The corresponding dose is about 0.2 Mrad/smy, and the equivalent 1-
216 MeV neutron fluence is about $5 \times 10^{11} \text{ n}_{\text{eq}}/\text{cm}^2/\text{smy}$ (smy: Snowmass Year =
217 10^7 sec). The long-term extrapolation of the beam background is affected by
218 large uncertainties from the optimization of collimator settings in MC and the
219 future evolution of the beam injection background, which is not simulated. This
220 uncertainty motivates the VXD upgrade which improves the tolerance of the hit
221 rates and the radiation damage, and the technology assessment is ongoing for
222 multiple sensor options.

223 From the measured dose on diamond sensors, the integrated radiation dose
224 in the layer-3 mid-plane sensors, which are the most exposed in the SVD,
225 is estimated to be 70 krad. The estimation is based on the correlation be-
226 tween the SVD occupancy and the diamonds dose. The estimated dose in-
227 cludes uncertainties of about 30% due to the unavailability of the appropri-
228 ate trigger before December 2020. Assuming the dose/ n_{eq} fluence ratio of
229 $2.3 \times 10^9 \text{ n}_{\text{eq}}/\text{cm}^2/\text{krad}$ from MC, 1-MeV equivalent neutron fluence is eval-
230 uated to be about $1.6 \times 10^{11} \text{ n}_{\text{eq}}/\text{cm}^2$ in the first two and a half years.

231 The effect of the integrated dose on the sensor leakage current is measured,
232 and the results show a clear linear correlation as in the upper plot of Fig. 6.
233 The slopes for all the sensors are summarized in the lower plot of Fig. 6. They
234 are around 2–5 $\mu\text{A}/\text{cm}^2/\text{Mrad}$. The large variations can be explained by tem-

235 perature effects and the deviation of sensor-by-sensor dose from the average in
236 each layer used in the estimation. The slopes are in the same order of magni-
237 tude as previously measured in the BaBar experiment [8], $1 \mu\text{A}/\text{cm}^2/\text{Mrad}$ at
238 20°C . While the leakage current is increasing, the impact on the strip noise is
239 suppressed by the short shaping time (50 ns) in APV25. It is expected to be
240 comparable to the strip-capacitive noise only after 10 Mrad irradiation and not
241 problematic for ten years where the integrated dose is estimated to be 2 Mrad.

242 The relation between the noise and the integrated dose is shown in Fig. 7.
243 The noise increase of 20–25% is observed in layer 3, but this does not affect the
244 SVD performance. This noise increase is likely due to the radiation effects on
245 the sensor surface. Fixed oxide charges on sensor surface increase non-linearly,
246 enlarging inter-strip capacitance. The noise saturation is observed on the v/n-
247 side and also starts to be seen on the u/p-side. This behavior agrees with the
248 increase of fixed oxide charges.

249 The full depletion voltage of the sensor is also a key property that can be
250 affected by the radiation damage. It can be measured from the v/n-side strip
251 noise, which suddenly decreases at the full depletion voltage because the sensor
252 substrate is n-type and thus the v/n-side strips can be fully isolated at the full
253 depletion. From this measurement, reasonable full depletion voltages, which are
254 consistent with the values mentioned in Sec. 2, were confirmed, and so far no
255 change in full depletion voltage is observed in the first two and a half years of
256 operation, which is consistent with the expectation from low integrated neutron
257 fluence of $1.6 \times 10^{11} \text{ n}_{\text{eq}}/\text{cm}^2$.

258 5. Conclusions

259 The SVD has been taking data in Belle II since March 2019 smoothly and
260 reliably. The detector performance is excellent and agrees with expectations.
261 We are ready to cope with the increased background during higher luminosity
262 running by rejecting the off-time background hits using hit-time and operating
263 in the three/six-mixed acquisition mode. In the recent study, the efficiency

264 loss in the three-samples data is confirmed to be less than 0.1% for the trigger
265 timing shift within ± 30 ns. The observed first effects of radiation damage are
266 also within expectation and do not affect the detector performance.

267 **Acknowledgments**

268 This project has received funding from the European Union’s Horizon 2020
269 research and innovation programme under the Marie Skłodowska-Curie grant
270 agreements No 644294 and 822070. This work is supported by MEXT, WPI,
271 and JSPS (Japan); ARC (Australia); BMFWF (Austria); MSMT (Czechia);
272 CNRS/IN2P3 (France); AIDA-2020 (Germany); DAE and DST (India); INFN
273 (Italy); NRF-2016K1A3A7A09005605 and RSRI (Korea); and MNiSW (Poland).

274 **References**

- 275 [1] T. Abe, et al., Belle II Technical Design Report (2010). arXiv:1011.0352.
- 276 [2] Y. Ohnishi, et al., Accelerator design at SuperKEKB, Prog. Theor. Exp.
277 Phys. 2013 (3), 03A011 (03 2013).
- 278 [3] S. Bacher, et al., Performance of the diamond-based beam-loss monitor sys-
279 tem of Belle II, Nucl. Instrum. Methods Phys. Res., Sect. A 997 (2021)
280 165157. arXiv:2102.04800.
- 281 [4] K. Adamczyk, et al., The belle ii silicon vertex detector assembly and me-
282 chanics, Nucl. Instrum. Methods Phys. Res., Sect. A 845 (2017) 38–42, pro-
283 ceedings of the Vienna Conference on Instrumentation 2016.
- 284 [5] M. J. French, et al., Design and results from the APV25, a deep sub-micron
285 CMOS front-end chip for the CMS tracker, Nucl. Instrum. Methods Phys.
286 Res., Sect. A 466 (2001) 359–365.
- 287 [6] G. Rizzo, et al., The Belle II Silicon Vertex Detector: Perform-
288 ance and Operational Experience in the First Year of Data Taking.
289 arXiv:<https://journals.jps.jp/doi/pdf/10.7566/JPSCP.34.010003>.

- 290 [7] R. L. Boucher, et al., Measurement of the cluster position resolution of the
291 Belle II Silicon Vertex Detector, these NIMA Conference Proceedings.
- 292 [8] B. Aubert, et al., The BaBar detector: Upgrades, operation and perfor-
293 mance, Nucl. Instrum. Methods Phys. Res., Sect. A 729 (2013) 615–701.

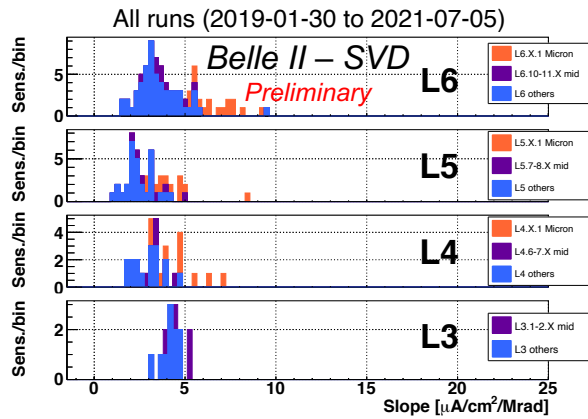
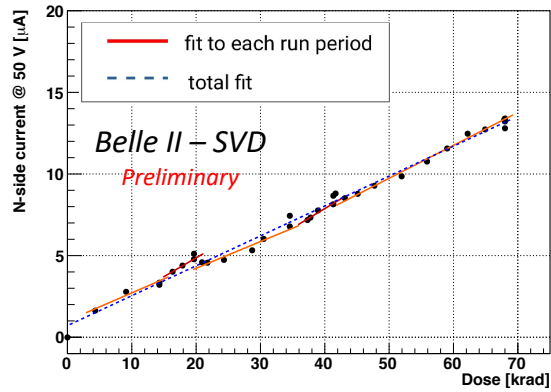


Figure 6: (upper) Effect of the integrated dose on the leakage current in the n/v-side of one layer-3 sensor. The slope is fitted for each run period (solid red line) and for all the runs (dashed blue line). Both fit results agree with each other and are consistent with the linear increase. (lower) The fit results of all the sensors for all runs. The sensors are classified as trapezoidal sensors in the forward region (Micron), sensors around the midplane, and the others.

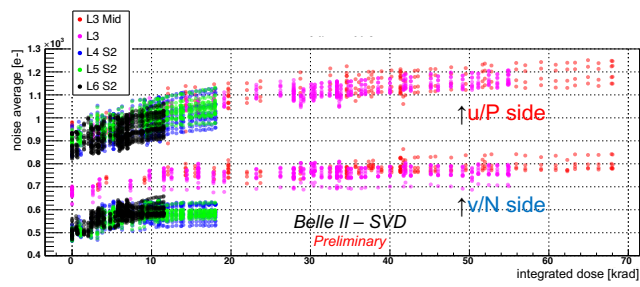


Figure 7: Effect of the integrated dose on the noise average in electron. The clear increase is observed and saturated (or start to be saturated) for layer-3 sensors.